


Please cite the Published Version

Uko, Mfonobong, Ekpo, Sunday , Enahoro, Sunday and Fanuel, Elias (2024) Performance Optimization Of 5G-Satellite Integrated Networks For IoT Applications: A Two-Ray Propagation Model Approach. Smart Cities, 7 (6). pp. 3895-3913. ISSN 2624-6511

DOI: <https://doi.org/10.3390/smartcities7060150>

Publisher: MDPI AG

Version: Published Version

Downloaded from: <https://e-space.mmu.ac.uk/637471/>

Usage rights:  [Creative Commons: Attribution 4.0](https://creativecommons.org/licenses/by/4.0/)

Additional Information: This is an open access article published in Smart Cities, by MDPI.

Data Access Statement: Data are contained within the article.

Enquiries:

If you have questions about this document, contact openresearch@mmu.ac.uk. Please include the URL of the record in e-space. If you believe that your, or a third party's rights have been compromised through this document please see our Take Down policy (available from <https://www.mmu.ac.uk/library/using-the-library/policies-and-guidelines>)

Article

Performance Optimization of 5G–Satellite Integrated Networks for IoT Applications in Smart Cities: A Two-Ray Propagation Model Approach

Mfonobong Uko ^{*,†} , Sunday C. Ekpo [†] , Sunday Enahoro [†] and Fanuel Elias 

Communication and Space Systems Engineering Research Team, Manchester Metropolitan University, Manchester M1 5GD, UK; s.ekpo@mmu.ac.uk (S.C.E.); sunday.enahoro@stu.mmu.ac.uk (S.E.); fanuel.elias@stu.mmu.ac.uk (F.E.)

* Correspondence: mfonuko12@gmail.com or m.uko@mmu.ac.uk

[†] These authors contributed equally to this work.

Highlights

What are the main findings?

- This study shows that lower satellite altitudes yield higher received power at short distances, making them better for short-range applications. For example, at 50 km, a 300 km altitude satellite achieves -115 dBm, compared to -136 dBm at 1000 km altitude. Beyond 2000 km, the altitude's effect diminishes, favouring higher altitudes for broad coverage.
- Frequency also plays an important role. Higher frequencies suffer more significant path loss over distance, balancing bandwidth efficiency and attenuation. At 1000 km, the received power at 24 GHz is -125 dBm versus -130 dBm at 32 GHz, showing the need to select frequencies carefully.
- While increasing bandwidth enhances capacity, distance reduces received power, limiting reliability. At 100 km, 50 MHz delivers 4500 Mbps, but only 300 Mbps at 3000 km. Outage probability rises at higher SNR thresholds: at 3000 km, a 15 dB threshold yields 25% outage versus less than 5% at 5 dB. Optimising SNR is critical for long-range performance.

What is the implication of the main finding?

- Lower satellite altitudes yield stronger signals at short distances, ideal for dense urban IoT. Higher altitudes enable wide coverage but weaker signals.
- Higher frequencies suffer more significant path loss, so frequency selection depends on the application: lower frequencies suit long links, and higher frequencies support high data rates at short ranges. Beamforming or boosted power can offset this loss. As distance increases, channel capacity declines, and outage probability rises, requiring dynamic resource management.
- Adjusting the bandwidth, lowering SNR thresholds, and using adaptive modulation and coding can be used to maintain reliability. This approach supports critical tasks like remote monitoring and emergency response across extended distances.

Abstract: The convergence of 5G terrestrial networks with satellite systems offers a revolutionary approach to achieving global, seamless connectivity, particularly for Internet of Things (IoT) applications in urban and rural settings. This paper investigates the implications of this 5G–satellite integrated network architecture, specifically through the application of the two-ray propagation model and the free-space path loss (FSPL) model. By simulating signal characteristics over varying distances, altitudes, and environmental parameters, we explore how factors such as transmitter height, satellite altitude, and frequency impact received power, path loss, channel capacity, and outage probability. The key findings indicate that received power decreases significantly with increasing distance, with notable oscillations in the two-ray model due to interference from ground reflections, particularly evident within the first 100 km. For example, at 50 km, a 300 km satellite altitude yields approximately -115 dBm in received power, while at 1000 km altitude, this power drops to around -136 dBm. Higher frequencies (e.g., 32 GHz) exhibit greater path loss than lower frequencies (e.g., 24 GHz), with a 5 dB difference observed at 1000 km, reinforcing the need for frequency considerations in long-range communication design. In terms of channel capacity, increasing bandwidth



Citation: Uko, M.; Ekpo, S.C.; Enahoro, S.; Elias, F. Performance Optimization of 5G–Satellite Integrated Networks for IoT Applications in Smart Cities: A Two-Ray Propagation Model Approach. *Smart Cities* **2024**, *7*, 3895–3913. <https://doi.org/10.3390/smartcities7060150>

Academic Editor: Pierluigi Siano

Received: 25 September 2024

Revised: 5 December 2024

Accepted: 9 December 2024

Published: 11 December 2024



Copyright: © 2024 by the authors. Licensee MDPI, Basel, Switzerland. This article is an open access article distributed under the terms and conditions of the Creative Commons Attribution (CC BY) license (<https://creativecommons.org/licenses/by/4.0/>).

enhances achievable data rates but declines with distance due to diminishing received power. At 100 km, a 50 MHz bandwidth supports up to 4500 Mbps, while at 3000 km, capacity drops to around 300 Mbps. The outage probability analysis shows that higher signal-to-noise ratio (SNR) thresholds substantially increase the likelihood of communication failures, especially at distances exceeding 2000 km. For instance, at 3000 km, the outage probability for a 15 dB SNR threshold reaches approximately 25%, compared to less than 5% for a 5 dB threshold. These results underscore the critical trade-offs in designing 5G–satellite IoT networks, balancing bandwidth, frequency, SNR thresholds, and satellite altitudes for optimal performance across diverse IoT applications. The analysis provides valuable insights for enhancing connectivity and reliability in 5G–satellite integrated networks, especially in remote and underserved regions.

Keywords: 5G networks; satellite systems; IoT applications; two-ray model; signal propagation

1. Introduction

The integration of 5G terrestrial networks with satellite systems presents a transformative opportunity to achieve seamless, ubiquitous connectivity on a global scale, particularly for the rapidly expanding Internet of Things (IoT) in smart cities [1–3]. As 5G technology continues to evolve, its promise of ultra-low latency, high data rates, and massive device connectivity can extend to areas traditionally underserved by terrestrial networks through the incorporation of satellite communication systems [4,5]. This 5G–satellite integrated network framework is poised to play a crucial role in enabling reliable communication in remote and rural areas, enhancing connectivity for critical applications such as autonomous vehicles, remote sensing, and global IoT networks [6,7].

The convergence of 5G and satellite systems introduces a new paradigm in communication infrastructure, merging the high-capacity, low-latency characteristics of 5G with the extensive coverage provided by satellite networks. This hybrid approach addresses the limitations of terrestrial-only networks, enabling continuous connectivity across challenging environments, including densely populated urban areas and isolated rural regions. For IoT applications in smart cities, this integration enables consistent, high-quality data exchange across a vast number of connected devices, essential for efficient urban management, environmental monitoring, and public safety [3,8].

Research in 5G–satellite convergence has gained considerable traction, focusing on the potential and challenges of integrating terrestrial and satellite networks for diverse applications. Kodheli et al. [9] highlight the technical challenges of integrating low-Earth-orbit (LEO) satellite networks with 5G, addressing issues such as handover mechanisms, interference management, and quality-of-service (QoS) maintenance. Zhu et al. [8] also discuss the architecture of integrated 5G–satellite networks, emphasizing the need for efficient resource allocation and interference coordination mechanisms to maintain reliable connectivity in high-density IoT deployments.

Existing studies have also addressed the unique propagation challenges posed by these networks, given the differing altitudes and coverage zones of terrestrial and satellite systems. Mohsan et al. [10] explore propagation characteristics specific to high-frequency bands in 5G and satellite communication, analysing how atmospheric absorption, scattering, and reflection impact signal quality. Their findings underline the importance of accounting for environmental factors, especially in dense urban settings where building interference and multipath effects are prevalent. Shinde et al. [11] propose adaptive modulation and coding techniques to mitigate propagation losses in hybrid networks, emphasizing the role of environment-specific models in ensuring robust performance.

A critical aspect of ensuring seamless connectivity in 5G–satellite integrated networks is the accurate modelling of signal propagation. The two-ray model has been widely used due to its simplicity and effectiveness in capturing the interaction between direct and reflected signals in terrestrial communication environments [12–14]. The model, which

considers both line-of-sight (LOS) and ground-reflected paths, is well suited for urban areas with significant ground infrastructure [12].

In the context of 5G–satellite convergence, however, using the two-ray model presents additional complexities due to varied altitudes and satellite signal paths. Kodheli et al. [9] suggest that while the two-ray model is beneficial for understanding ground-based reflections in 5G–satellite integrated networks, it requires further adaptation to account for factors such as signal delay, Doppler shift, and the Earth’s curvature. Recent works by Moraitis et al. [15] propose modified versions of the two-ray model, incorporating satellite-specific propagation characteristics, thereby improving predictive accuracy in 5G–satellite integrated networks.

The use of 5G–satellite networks in IoT applications, especially within smart cities, introduces unique challenges that necessitate further research. Colding et al. [1] argue that integrating satellite connectivity in urban IoT frameworks requires careful planning to address interference from dense infrastructure, high device density, and environmental variability. Wang et al. [2] discuss the technical implications of IoT applications in 5G–satellite integrated networks, focusing on stringent latency and reliability requirements for real-time applications like traffic monitoring, public safety, and energy management.

Recent studies highlight the need for adaptive network control mechanisms to dynamically manage resource allocation and optimize connectivity. Uko et al. [16] and Bellini et al. [17] suggest that 5G–satellite integrated networks for IoT in smart cities can benefit from algorithms for dynamic power adjustment, interference cancellation, and multipath routing, aiming to optimize network efficiency and resilience, especially where terrestrial support is limited. Advanced AI-driven approaches, as discussed by Shinde et al. [11], show promise for managing complex, real-time network adjustments, enhancing system adaptability to fluctuating environmental and traffic conditions.

Building upon the established foundation of 5G–satellite convergence research, this study enhances the two-ray propagation model to incorporate complex environmental attenuation factors, such as rain and atmospheric absorption, that significantly impact high-frequency signals typical of 5G and satellite communications [18]. These factors are critical in modelling real-world scenarios accurately, especially at millimetre-wave (mmWave) frequencies, where propagation losses due to rain and atmospheric gases become pronounced [19–21].

We integrate the ITU-R rain attenuation model, which provides frequency-dependent attenuation based on the rain rate and path length, significantly affecting the signal strength under high rain conditions [22]. Additionally, we incorporate atmospheric absorption for oxygen and water vapour, critical for high-frequency bands in 5G and satellite communications, calculated based on ITU-R recommendations to account for temperature, humidity, and pressure variations along the path.

Unlike previous studies focusing on terrestrial or satellite-only propagation, our work delves into how altitude, distance, and environmental reflections impact signal quality in 5G–satellite networks. These novel components enable a more comprehensive analysis of real-world signal behaviour, offering valuable insights for designing and optimizing robust hybrid communication networks for IoT applications in urban smart cities and remote regions.

This paper extends the application of the two-ray model to 5G–satellite convergence, with a specific focus on its implications for signal strength and quality under realistic environmental conditions. Section 2 provides a review on 5G and satellite network convergence, summarizing existing studies and the literature. In Section 3, we introduce the enhanced two-ray model that includes rain attenuation and atmospheric absorption. We analyse the model’s predictive capability in identifying areas of constructive and destructive interference, crucial for designing resilient hybrid systems. Section 4 presents the results, offering insights into optimizing 5G–satellite integrated networks capable of supporting diverse IoT applications in a 5G–satellite smart city. Section 5 shows analytical validation of our proposed framework and Section 6 gives the conclusions from our findings.

2. Integrating 5G and Satellite Networks for Enhanced IoT Applications in Smart Cities: A Review

The convergence of 5G and satellite networks represents a significant advancement in telecommunications, combining the unique strengths of terrestrial and satellite systems to provide extensive coverage, improved connectivity, and reliability across various environments [23–25]. By integrating satellite networks, 5G technology overcomes the constraints of terrestrial infrastructure, enabling fast, responsive communication in remote and hard-to-reach areas, including oceans, airborne platforms, and space-borne environments. This hybrid approach is particularly advantageous for the Internet of Things (IoT), which demands reliable, widespread connectivity for various applications, from basic sensors to advanced autonomous systems [26].

The Internet of Things (IoT) comprises an expansive array of devices, including everything from simple environmental sensors to sophisticated autonomous vehicles and industrial automation systems [27,28]. Consistent communication across different environments is critical to IoT functionality, especially in smart cities where large data volumes must be transmitted in real-time for urban management, environmental monitoring, and public safety. The 5G–satellite integrated network provides an ideal solution by leveraging the high data rates and low latency of 5G in dense urban areas, while satellite coverage ensures connectivity in remote regions where terrestrial infrastructure is sparse [29,30].

The integration of 5G and satellite networks requires careful consideration of each system's distinct propagation characteristics. Primarily operating in the millimetre-wave (mmWave) spectrum, 5G utilizes frequencies between 24 GHz and 52 GHz, offering high data speeds but suffering from significant path loss in non-line-of-sight (NLOS) scenarios [31].

In real-world settings, the propagation environment includes not only direct line-of-sight (LOS) components but also multiple scattered components resulting from reflection, diffraction, and scattering. The Rician fading model, characterized by the Rician K -factor, is suitable for scenarios where both LOS and scattered components significantly impact signal strength [32].

High-frequency satellite communications, especially those in the Ka-band (26.5 GHz to 40 GHz) and V-band (40 GHz to 75 GHz), are subject to additional attenuation due to atmospheric gases and rain, critical factors that must be integrated into propagation models. The ITU-R models for rain attenuation and gaseous absorption provide frequency-dependent attenuation factors, allowing for more accurate modelling of signal degradation in hybrid environments [33,34].

The two-ray model is commonly used to predict signal path loss by considering both direct and ground-reflected paths. Optimizing data transmission in 5G–satellite networks also requires efficient modulation schemes. Quadrature amplitude modulation (QAM) is widely used in both 5G and satellite communications due to its high spectral efficiency. The spectral efficiency η of an M -ary QAM system can be expressed as

$$\eta = \log_2(M) \text{ bits/s/Hz} \quad (1)$$

with the effective data rate R defined as

$$R = \eta \cdot B = \log_2(M) \cdot B \quad (2)$$

where B is the channel bandwidth. Higher-order QAM schemes, such as 64-QAM and 256-QAM, provide increased data rates but require higher signal-to-noise ratios (SNRs) to maintain reliability, making them susceptible to rain attenuation and atmospheric absorption effects [34].

The integration of these factors—FSPL, Rician fading, atmospheric absorption, rain attenuation, and the two-ray model—yields a comprehensive propagation framework for 5G–satellite networks. The proposed model provides a holistic approach to capturing signal variations across different environments, frequencies, and atmospheric conditions. By including rain and atmospheric attenuation factors alongside traditional propagation models,

this approach allows for better accuracy in predicting signal strength, which is crucial for IoT applications in 5G–satellite integrated networks. This model supports the design of resilient communication systems, enabling IoT deployments that can withstand varied environmental conditions and maintain connectivity, thereby enhancing the network’s robustness in both urban and remote areas.

3. Enhanced Mathematical Model with Atmospheric and Environmental Effects

A 5G–satellite integrated network requires accurate modelling of signal propagation effects across large distances, incorporating environmental variability between satellites and terrestrial receivers. Traditional models like free-space path loss (FSPL), the two-ray model, and Rician fading provide a foundation but lack the complexity needed to address factors such as atmospheric and rain attenuation, which are critical in high-frequency 5G and satellite communications. In this enhanced model, we integrate these environmental elements to develop a comprehensive framework for 5G–satellite IoT applications, enabling a robust analysis of real-world signal dynamics.

3.1. Two-Ray Model Overview

The two-ray model considers both the direct line-of-sight (LOS) signal and a reflected non-line-of-sight (NLOS) signal (as shown in Figure 1). This model is particularly significant in analysing and predicting the behaviour of radio wave propagation in scenarios where both direct and reflected signals contribute to the received signal [12–14]. In such scenarios, especially in environments with large reflective surfaces like oceans or flat terrain, the two-ray model becomes crucial for accurately modelling signal strength, fading, and phase shift, which are all important factors for reliable communication between the ground station and the low-Earth-orbit (LEO) satellite [23].

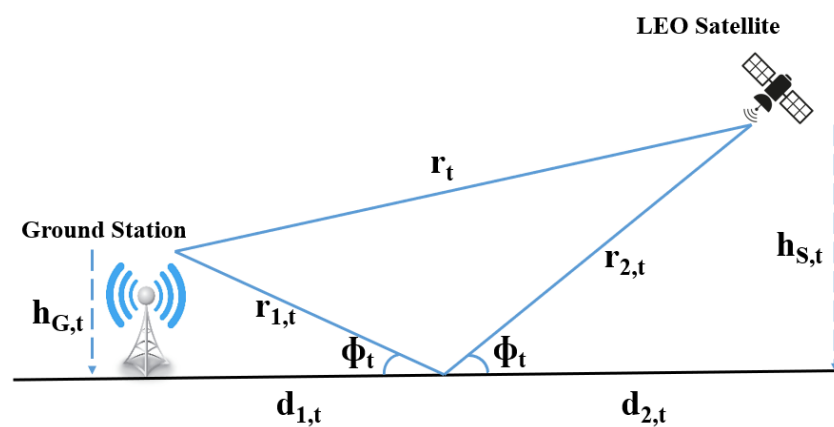


Figure 1. Two-ray geometry for 5G–satellite network.

In the two-ray geometry model, the signal from a transmitter (e.g., a ground station) to a receiver (e.g., a satellite) reaches the receiver through two distinct paths:

1. **Direct path (r_t):** This is the line-of-sight (LOS) path that directly connects the ground station to the satellite.
2. **Ground station reflected path ($r_{1,t}$):** This path involves the signal reflecting off the Earth’s surface before reaching the ground station.
3. **Satellite reflected path ($r_{2,t}$):** This path involves the signal reflecting off the Earth’s surface before reaching the satellite.

The constructive or destructive interference of these components is determined by the phase difference between them, resulting in either signal augmentation or fading.

3.2. Enhanced Two-Ray Model with Atmospheric and Rain Attenuation

For the hybrid model, we extend the two-ray model with atmospheric and rain attenuation, suitable for long-range, high-altitude propagation in 5G-satellite communication.

Given a ground station height $h_{G,t}$, satellite height $h_{S,t}$, and distances $r_{1,t}$ and $r_{2,t}$:

$$r_{1,t} = \sqrt{(d_{1,t} + d_{2,t})^2 + (h_{S,t} - h_{G,t})^2} \quad (3)$$

$$r_{2,t} = \sqrt{(d_{1,t} + d_{2,t})^2 + (h_{S,t} + h_{G,t})^2} \quad (4)$$

Including atmospheric and rain attenuation, the received power for each path is

$$P_{r,1} = P_t \left(\frac{\lambda}{4\pi r_{1,t}} \right)^2 e^{-(A_{\text{atm}} + \gamma_r) \cdot r_{1,t}} \quad (5)$$

$$P_{r,2} = P_t \left(\frac{\lambda}{4\pi r_{2,t}} \right)^2 \Gamma e^{-(A_{\text{atm}} + \gamma_r) \cdot r_{2,t}} \quad (6)$$

where Γ is the reflection coefficient based on surface characteristics. The total received power P_r is

$$P_r = |E_{r,1} + E_{r,2} e^{j\Delta\phi}|^2 = P_{r,1} + |\Gamma|^2 P_{r,2} + 2\sqrt{P_{r,1} P_{r,2}} \cos(\Delta\phi) \quad (7)$$

Here, $\Delta\phi$ is the phase difference, which accounts for Doppler shifts and other delays.

3.3. Free-Space Path Loss (FSPL) with Atmospheric Attenuation

The FSPL model describes basic signal attenuation over a distance d in a vacuum, given by

$$\text{FSPL}(dB) = 20 \log_{10} \left(\frac{4\pi d f}{c} \right) \quad (8)$$

where f is the frequency, c is the speed of light, and d is the distance between the transmitter and receiver. To incorporate real-world environmental losses, we add atmospheric attenuation, particularly relevant at high frequencies. The FSPL with atmospheric attenuation FSPL_{atm} is given by

$$\text{FSPL}_{\text{atm}}(dB) = 20 \log_{10} \left(\frac{4\pi d f}{c} \right) + A_{\text{atm}} \cdot d \quad (9)$$

where A_{atm} is the atmospheric attenuation factor in dB/km. Atmospheric attenuation, denoted as A_{atm} , is primarily affected by two components: the dry air attenuation coefficient, $\alpha_{\text{dry}}(f)$; and the water vapour attenuation coefficient, $\alpha_{\text{wet}}(f)$. These components are frequency-dependent, and their combined effect over a distance d can be modelled by the equation

$$A_{\text{atm}}(f, d) = (\alpha_{\text{dry}}(f) + \alpha_{\text{wet}}(f)) \cdot d \quad (10)$$

where f is the signal frequency. Both $\alpha_{\text{dry}}(f)$ and $\alpha_{\text{wet}}(f)$ tend to increase with frequency, leading to higher attenuation levels as f rises. This relationship underscores the vulnerability of higher frequencies to atmospheric effects, especially over extended distances.

3.4. Rain Attenuation Model

Rain introduces significant attenuation, especially in high-frequency bands (Ka and V bands), often used in satellite communications. Rain attenuation A_{rain} is modelled as

$$A_{\text{rain}}(dB) = \gamma_r \cdot d \quad (11)$$

where γ_r is the specific attenuation coefficient in dB/km, dependent on rainfall intensity R (mm/h). The coefficient γ_r is calculated using the ITU-R P.838 model:

$$\gamma_r = kR^\alpha \quad (12)$$

where k and α are empirically derived parameters, varying with frequency and polarization. Thus, the FSPL with both atmospheric and rain attenuation is

$$\text{FSPL}_{\text{rain}}(\text{dB}) = 20 \log_{10} \left(\frac{4\pi df}{c} \right) + A_{\text{atm}} \cdot d + kR^\alpha \cdot d \quad (13)$$

This model comprehensively accounts for atmospheric and rain effects, making it suitable for 5G–satellite IoT link assessment.

3.5. Rician Fading with Atmospheric and Rain Attenuation

To model scattering effects beyond LOS, we incorporate a Rician fading model, where K represents the LOS-to-scattered power ratio. The Rician fading model under atmospheric and rain attenuation is given by

$$P_r = P_{\text{LOS}} \left(\frac{\lambda}{4\pi d} \right)^2 e^{-(A_{\text{atm}} + \gamma_r) \cdot d} \cdot (K + 1) \cdot e^{-\sigma^2 K} \quad (14)$$

where P_{LOS} is the LOS power, σ^2 is the variance of the Gaussian-distributed scattered component, and d is the path distance.

3.6. Combined Received Power for 5G–Satellite Links

The combined received power integrating the FSPL, two-ray, and Rician fading models with atmospheric and rain effects is

$$P_r = \left| \left(\frac{P_t \lambda}{4\pi r_{1,t}} \right)^2 e^{-(A_{\text{atm}} + \gamma_r) \cdot r_{1,t}} + \Gamma \left(\frac{P_t \lambda}{4\pi r_{2,t}} \right)^2 e^{-(A_{\text{atm}} + \gamma_r) \cdot r_{2,t}} \right|^2 + P_{\text{scattered}} \quad (15)$$

where $P_{\text{scattered}}$ represents non-LOS scattering, calculated by integrating the Rician model.

3.7. Channel Capacity and Outage Probability with Environmental Effects

Channel capacity C , using the Shannon–Hartley theorem, is

$$C = B \log_2 \left(1 + \frac{P_r}{N_0} \right) \quad (16)$$

For multipath scenarios, effective channel capacity C_{eff} over distance D is

$$C_{\text{eff}} = B \int_0^D \log_2 \left(1 + \frac{P_r(d)}{N_0} \right) dd \quad (17)$$

Outage probability P_{out} , the likelihood that SNR γ falls below threshold γ_{th} , is

$$P_{\text{out}} = 1 - e^{-\frac{\gamma_{\text{th}}}{\gamma}} \quad (18)$$

This model provides a comprehensive framework to assess 5G–satellite integrated networks, accommodating diverse propagation phenomena crucial for reliable IoT and urban applications under various environmental conditions.

4. A 5G–Satellite Convergence Analysis: Practical Considerations for IoT Applications in Smart Cities

The following results illustrate the performance and signal characteristics of a 5G–satellite integrated network using the two-ray model and free-space path loss (FSPL) model. Parameters such as satellite height, frequency, transmitter height, and dielectric constant were varied to observe their impact on received power, path loss, reflection coefficient,

channel capacity, and outage probability. The simulation was conducted with the following parameters in Table 1 to model the two-ray propagation and free-space path loss (FSPL):

Table 1. Simulation parameters for enhanced 5G–satellite propagation model.

Parameter	Value(s)
Satellite Altitudes	300 km, 500 km, 700 km, 1000 km
Frequency Bands	24 GHz, 28 GHz, 32 GHz
Bandwidths	10 MHz, 20 MHz, 50 MHz
Distance Range	0–3000 km
Transmitter Height (h_t)	30 m
Receiver Heights (h_r)	1.5 m (Low Rx), 100 m (High Rx)
Effective Earth Radius (R_e)	6371 km
Dielectric Constant (ϵ_r)	15
Noise Power Spectral Density (N_0)	−174 dBm/Hz
SNR Thresholds	5 dB, 10 dB, 15 dB
Atmospheric Attenuation Factors (A_{atm})	Calculated as $\alpha_{\text{dry}}(f) + \alpha_{\text{wet}}(f)$
Dry Atmospheric Absorption ($\alpha_{\text{dry}}(f)$)	Frequency-dependent, per ITU-R P.676
Wet Atmospheric Absorption ($\alpha_{\text{wet}}(f)$)	Frequency-dependent, per ITU-R P.676
Rainfall Intensity (R)	0–50 mm/h
Rain Attenuation Coefficient (γ_r)	kR^α (parameters from ITU-R P.838)
Rician K -factor	3, 6, 10

4.1. Performance Analysis of Atmospheric Attenuation in 5G–Satellite Integrated Networks

Figure 2 provides key insights into the influence of frequency, altitude, and distance on atmospheric attenuation in 5G–satellite integrated networks. This understanding is crucial for optimizing the network design, particularly in high-frequency 5G bands, where signal loss due to atmospheric effects can be substantial.

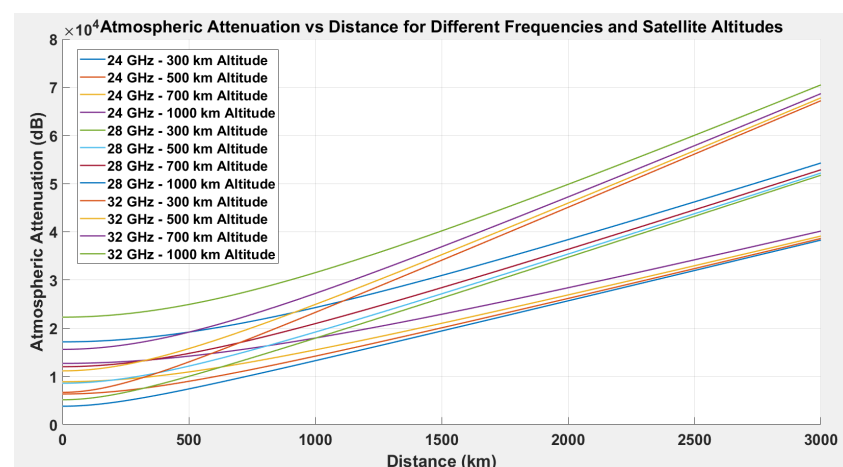


Figure 2. Atmospheric attenuation vs. distance for different frequencies and satellite altitudes.

The plot illustrates that as frequency increases from 24 GHz to 32 GHz, atmospheric attenuation grows considerably, particularly at longer distances. This behaviour is due to the proportional relationship between attenuation coefficients and frequency, given by

$$\alpha(f) \propto f \quad (19)$$

This implies that, for a fixed distance d , higher-frequency signals (such as those at 32 GHz) experience greater atmospheric attenuation than lower-frequency signals (e.g., 24 GHz). This trend is clearly visible in the plot, where the attenuation curves for 32 GHz are consistently higher than those for 24 GHz across all altitudes, highlighting the frequency-dependent nature of atmospheric losses.

Another critical factor influencing atmospheric attenuation is the altitude of the satellite. The plot includes data for four distinct satellite altitudes: 300 km, 500 km, 700 km, and 1000 km. Lower altitudes are associated with higher attenuation, especially over long distances. This is because lower altitudes imply a denser atmospheric path, increasing the probability of molecular absorption and scattering. For a satellite at altitude h , the effective path length through the atmosphere d_{eff} reduces as h increases, leading to the following expression:

$$A_{\text{atm}} \approx (\alpha_{\text{dry}}(f) + \alpha_{\text{wet}}(f)) \cdot d_{\text{eff}} \quad (20)$$

where d_{eff} is shorter for higher altitudes, thereby reducing cumulative attenuation. Consequently, satellites positioned at 1000 km experience lower attenuation compared to those at 300 km, as seen in the plot.

Figure 2 further reveals a nearly linear increase in attenuation with distance for a fixed frequency and altitude, which is consistent with the linear dependence on d . However, the combination of high frequency (such as 32 GHz) and low altitude (e.g., 300 km) results in a substantial amplification of attenuation, suggesting an almost multiplicative effect of frequency and altitude on atmospheric losses.

At shorter distances (less than 500 km), the variation in attenuation across different altitudes is minimal. However, as the distance extends, the separation between curves becomes more pronounced. For instance, at 3000 km, the attenuation for a 32 GHz signal at 300 km altitude approaches 8×10^4 dB, whereas a 24 GHz signal at 1000 km altitude remains significantly lower. This demonstrates that optimal frequency and altitude selection are crucial for long-distance 5G-satellite links, especially for IoT applications that require reliable connectivity for smart cities.

The observed relationships among frequency, altitude, and distance have several implications for network design:

- **Frequency selection:** Lower frequencies (e.g., 24 GHz) are preferable for long-distance communications, especially at lower altitudes, to mitigate atmospheric attenuation.
- **Altitude optimization:** Higher satellite altitudes reduce atmospheric losses, making them more suitable for high-frequency or long-range communications.
- **Distance constraints:** For applications that demand very long range communication, managing attenuation through optimal selection of altitude and frequency becomes essential to ensure sufficient signal strength.

In summary, the plot highlights the complex trade-offs between frequency, distance, and altitude in the design of 5G-satellite networks. A balanced approach to selecting these parameters can enhance network performance, a necessity for the scalability and reliability of IoT applications in a smart city.

4.2. Analysis of Rain Attenuation in 5G-Satellite Integrated Networks

The plot in Figure 3 illustrates the rain attenuation versus distance across different frequencies (24 GHz, 28 GHz, and 32 GHz) and rain rates (5 mm/h, 10 mm/h, 20 mm/h, and 50 mm/h). This analysis provides insights into the impact of rain on signal attenuation in 5G-satellite networks, particularly for high-frequency bands commonly utilized in satellite communications. As shown, rain attenuation increases significantly with both frequency and rainfall intensity, highlighting the challenges posed by adverse weather conditions in maintaining reliable communication links over long distances.

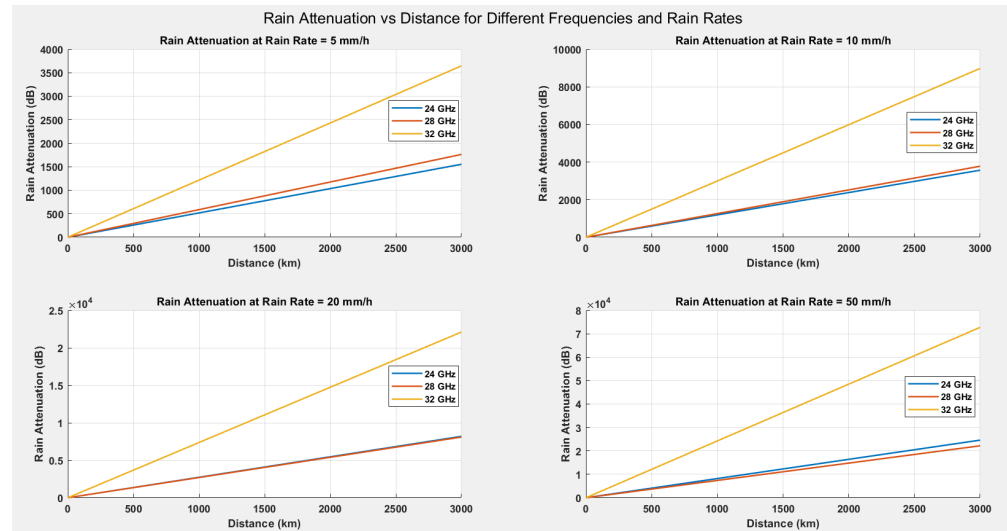


Figure 3. Rain attenuation vs. distance for different frequencies and rain rates.

The linear relationship between A_{rain} and d implies that for a given rain rate and frequency, attenuation increases proportionally with distance. This is evident across all plots in Figure 3, where the attenuation curves exhibit a linear trend as distance extends from 0 to 3000 km.

Higher frequencies result in greater rain attenuation, as demonstrated by the separation of curves for 24 GHz, 28 GHz, and 32 GHz. This effect is due to the proportional relationship between the frequency and the attenuation coefficient γ_r , which generally increases with frequency. At a given rain rate, the 32 GHz signal experiences the highest attenuation, followed by 28 GHz and 24 GHz. For instance, at a rain rate of 5 mm/h and a distance of 3000 km, the rain attenuation at 32 GHz reaches nearly 4000 dB, while at 24 GHz, it remains below 2000 dB. This demonstrates that for long-distance communication, higher frequencies suffer considerably more loss due to rain attenuation, making them less suitable for adverse weather conditions.

The influence of rain rate on attenuation is also apparent in Figure 3. As the rain rate increases from 5 mm/h to 50 mm/h, the attenuation grows substantially for all frequencies. The relationship between rain rate R and specific attenuation γ_r follows a power-law function $\gamma_r = kR^\alpha$, meaning that even small increases in R can lead to significant rises in γ_r , particularly at higher frequencies where k and α are larger. This phenomenon is evident at a rain rate of 50 mm/h, where attenuation at 32 GHz approaches 8×10^4 dB at a distance of 3000 km, compared to about 1.5×10^4 dB at 24 GHz under the same conditions.

The observed pattern indicates that the rain rate plays a critical role in determining signal loss. For example, in a heavy-rain scenario (50 mm/h), even a lower-frequency signal like 24 GHz experiences severe attenuation, which can reach values around 1.5×10^4 dB over long distances. Thus, rain intensity directly impacts link reliability, especially in high-frequency bands where attenuation is already exacerbated by frequency-dependent factors.

The analysis of rain attenuation reveals essential considerations for 5G-satellite networks, particularly in regions prone to heavy rainfall. Higher frequencies, such as 32 GHz, though useful for bandwidth efficiency, may not be viable for long distances or high-rainfall areas due to the high attenuation values observed. Instead, lower frequencies like 24 GHz, while still impacted by rain, offer relatively lower attenuation, suggesting a trade-off between data rate and weather resilience.

For IoT applications in smart cities, this trade-off is significant. In dense urban areas, where high-frequency bands are preferred for their data handling capabilities, the presence of rain can substantially degrade the link quality, impacting real-time data transmission essential for critical services. To mitigate this, adaptive frequency management, such as dynamically shifting to lower frequencies during heavy rain, could be implemented to sustain network reliability.

4.3. Effect of Satellite Height on Received Power

Figure 4 illustrates the relationship between satellite height and received power over a range of distances in the two-ray model. In this model, received power is influenced by the path length and ground reflection effects. As the height of the satellite increases from 300 km to 1000 km, the received power generally decreases, particularly at shorter distances. This is due to the increased path length associated with higher altitudes, which leads to greater free-space path loss and a reduced influence of ground reflections.

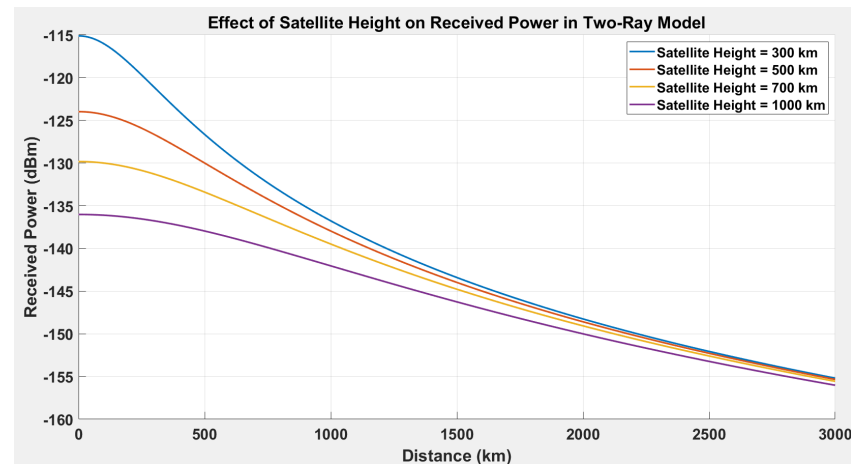


Figure 4. Effect of satellite height on received power in two-ray model.

As distance increases, the received power values for different satellite heights converge. Beyond 2000 km, the differences between satellite heights become less noticeable, with all curves following a similar decreasing trend. For instance, at a distance of 2500 km, the received power for a satellite height of 300 km is approximately -153 dBm, while it is about -154 dBm for a satellite height of 700 km. This indicates that at greater distances, the dominant factor influencing received power is the path length, and the impact of satellite height diminishes. This trend suggests that for applications requiring connectivity over very long distances, the choice of satellite height has a smaller effect on received power compared to applications with shorter ranges.

Figure 5 provides a closer examination of received power at shorter distances (up to 100 km) across different satellite heights. Here, the differences in received power due to satellite height are particularly evident. For instance, at a distance of 50 km, the received power for a satellite height of 300 km is approximately -115 dBm, while it is around -124 dBm, -129 dBm, and -136 dBm for satellite heights of 500 km, 700 km, and 1000 km, respectively. This detailed view highlights that lower satellite altitudes provide substantially higher received power at short distances, making them preferable for applications where high power levels and signal strength are critical over short ranges.

These findings suggest that lower satellite altitudes are advantageous for applications requiring robust signal strength at shorter distances, such as IoT deployments, remote sensing, and certain emergency communications, where reliable connectivity is required within a limited area. However, for applications focused on wide-area coverage over long distances, higher satellite altitudes may be sufficient, as the effect of height on received power becomes less significant at extended ranges.

Figure 6 provides a heatmap of received power across varying distances and satellite heights. As the satellite height increases, received power decreases, with more pronounced losses at longer distances. This heatmap offers a comprehensive visualization, supporting system design decisions regarding optimal satellite height based on coverage area and power requirements.

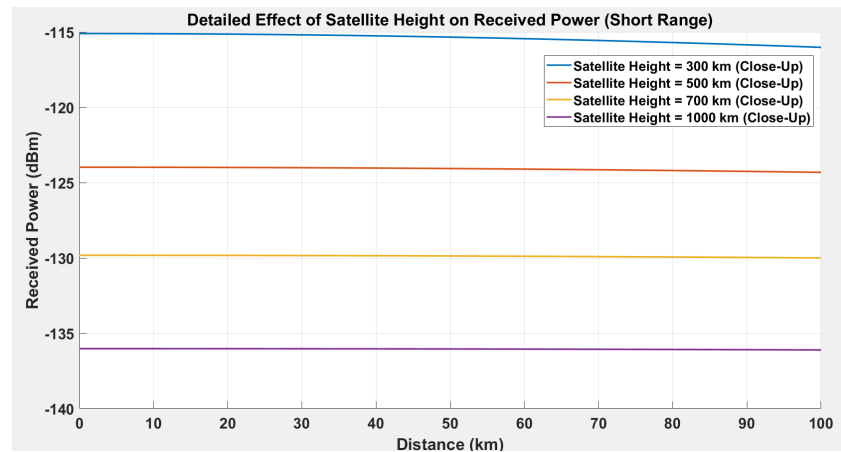


Figure 5. Effect of satellite height on received power (short range).

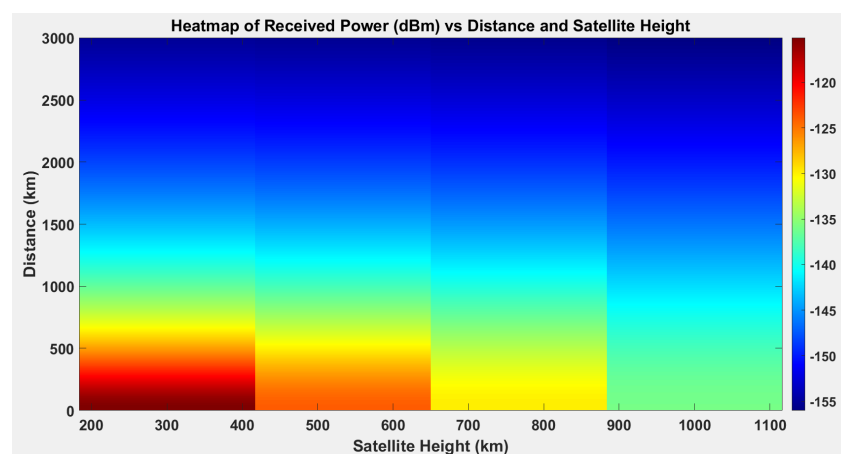


Figure 6. Heatmap of received power (dBm) vs. distance and satellite height.

4.4. Received Power vs. Distance Across Frequencies in the FSPL Model

Figure 7 illustrates the impact of frequency on received power. The analysis compares three frequencies: 24 GHz, 28 GHz, and 32 GHz, which represent typical 5G mmWave frequencies. The results clearly show that higher frequencies are associated with increased path loss, particularly over longer distances, due to the relationship between frequency and free-space attenuation.

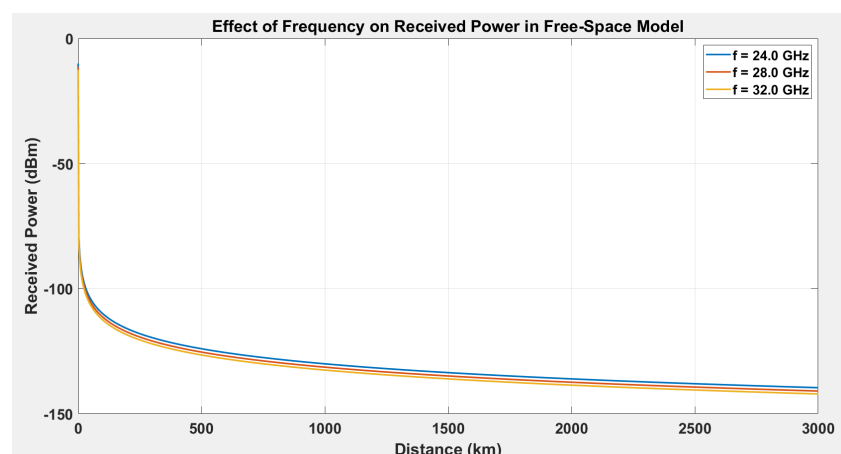


Figure 7. Effect of frequency on path loss in free-space model.

At 1000 km, the received power at 24 GHz is approximately -125 dBm, whereas it drops to around -128 dBm at 28 GHz and -130 dBm at 32 GHz. This 5 dB difference between 24 GHz and 32 GHz highlights the increasing sensitivity of higher frequencies to path loss over longer distances. By 3000 km, the received power at 24 GHz falls to around -145 dBm, while at 28 GHz and 32 GHz, it reaches approximately -148 dBm and -150 dBm, respectively. The cumulative increase in path loss with frequency becomes evident over long-range communication, as higher frequencies experience greater attenuation.

4.5. Path Loss vs. Transmitter–Receiver (Tx–Rx) Separation Distance

Figures 8 and 9 model compare different path loss models as a function of the transmitter–receiver (Tx–Rx) separation distance. These models illustrate the path loss for both high and low receiver antenna heights using various path loss models. The two-ray model is employed to account for the ground reflection in addition to the direct LOS path. This model is calculated separately for high and low receiver heights to observe how the reflection affects path loss at different altitudes.

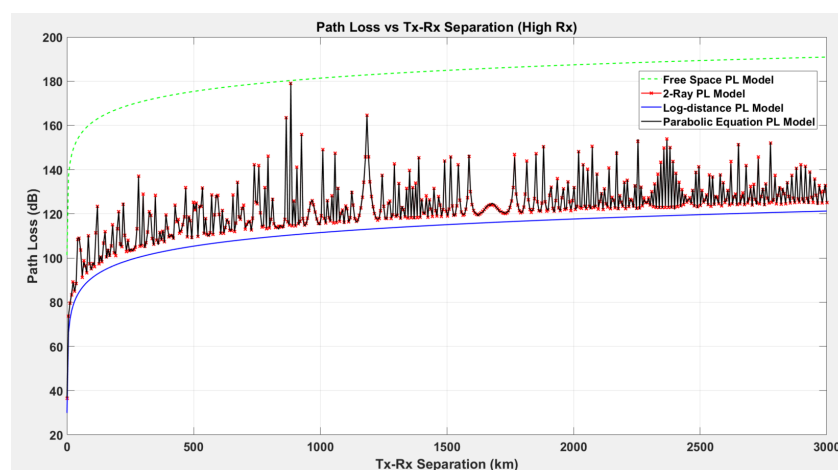


Figure 8. Path loss vs. Tx–Rx separation (high Rx).

Figure 8 illustrates the relationship between path loss and the separation distance between the transmitter (Tx) and receiver (Rx) for a high receiver height. The graph is essential for comprehending the predictions of route loss by different propagation models at different distances, particularly in situations with raised receiver positions. This is particularly critical for 5G–satellite network applications and elevated terrestrial receivers. The FSPL model, is the simplest model and serves as a baseline, showing a continuous and gradual increase in path loss as the Tx–Rx separation increases. The two-ray model, shown by the red curve, considers both the direct path and a reflected path (typically from the ground) between the transmitter and receiver. This model introduces a more complex behaviour, particularly noticeable in the oscillatory pattern of the path loss. The periodic fluctuations are due to constructive and destructive interference between the direct and reflected paths, which result in alternating regions of higher and lower path loss. This model is particularly important in environments where ground reflection plays a significant role.

Furthermore, from Figure 8, the log-distance path loss model, depicted by the blue curve, is a more empirical model that accounts for factors like the environment and the terrain. It shows a more gradual increase in path loss compared to the FSPL model and tends to be smoother than the two-ray model. This model is vital for analysing urban or suburban environments where multiple obstacles affect the signal propagation. The high receiver height in this simulation likely reduces the impact of ground reflections to some extent, as indicated by the fact that the two-ray model's oscillations decrease in amplitude as distance increases. However, the high receiver height also means that any interference effects are more pronounced over longer distances, as the direct and reflected paths can differ significantly in length, leading to greater phase differences. The two-ray model's

ability to predict the oscillatory behaviour of path loss due to multipath interference is crucial for designing robust communication links, particularly in 5G–satellite integrated networks, where such effects can be pronounced. This model is particularly relevant for ground stations communicating with satellites, where reflections from the ground or water surfaces can lead to significant variations in signal strength.

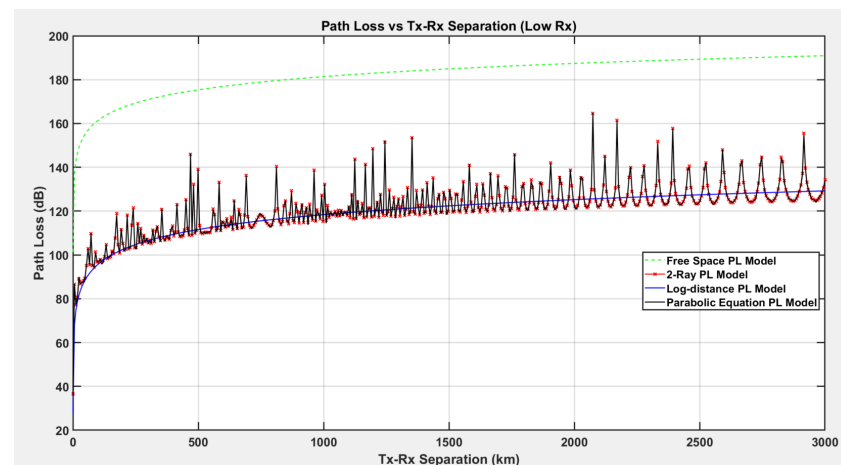


Figure 9. Path loss vs. Tx-Rx separation (low Rx).

Figure 9 provides a detailed analysis of the path loss experienced at various separation distances between the transmitter (Tx) and receiver (Rx) when the receiver is at a lower elevation. This is crucial for understanding how different propagation models behave under the condition of a low receiver height, which is a common scenario in ground-based IoT devices or terrestrial communication systems. The analysis involves comparing several path loss models, namely, the free-space path loss (FSPL) model, the two-ray model, the log-distance path loss model, and the parabolic equation path loss model. The FSPL model is represented by the green dashed line and assumes an idealized scenario where the signal propagates in a straight line through free space without any obstructions or reflections. The path loss increases steadily with the distance between the Tx and Rx. This model is often used as a baseline because it only considers the distance and frequency but not the environment. The two-ray model is shown with the red curve. This model accounts for both the direct path and a reflected path (typically from the ground) between the transmitter and the receiver. The characteristic feature of this model is the oscillatory behaviour in the path loss curve, which results from constructive and destructive interference between the direct and reflected signals. The oscillations are particularly pronounced at shorter distances and gradually diminish as the distance increases. This behaviour is due to the phase difference between the direct and reflected paths becoming more significant at shorter ranges.

With a low Rx height, ground reflections play a significant role, as evidenced by the pronounced oscillations in the two-ray model. This suggests that in low-height applications, such as ground-based IoT devices, reflections from the ground or nearby surfaces can lead to significant variations in signal strength, potentially causing areas of strong signal (constructive interference) or weak signal (destructive interference). The low Rx height also means that the effective path difference between the direct and reflected waves is smaller, leading to more frequent interference patterns. This is particularly important when designing systems for ground-based applications, where maintaining consistent signal strength is crucial for reliable communication.

4.6. Channel Capacity vs. Distance with Bandwidth Variations

Figure 10 illustrates the relationship between channel capacity and distance for three different bandwidths: 10 MHz, 20 MHz, and 50 MHz. Channel capacity is a critical metric for applications that require high data rates, such as Internet of Things (IoT) devices com-

municating over satellite links. As expected, channel capacity increases with bandwidth, highlighting the benefits of allocating wider bandwidths to support high-data-rate requirements. However, the capacity decreases significantly with distance due to the reduction in received power, demonstrating the impact of path loss over extended ranges.

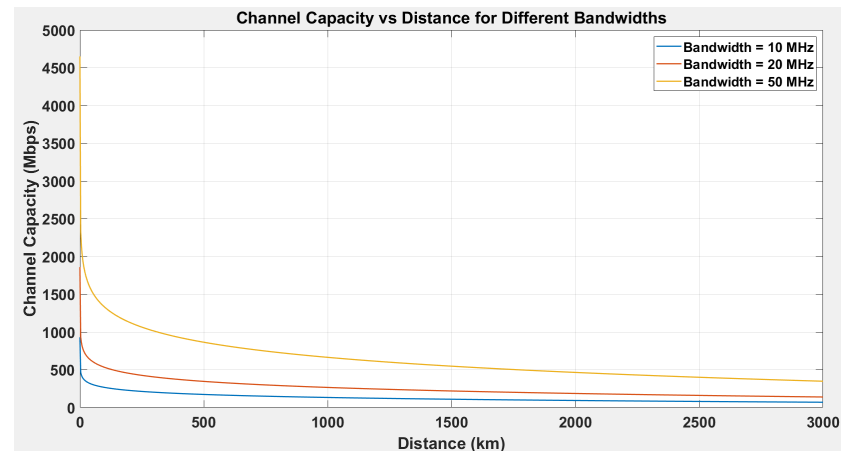


Figure 10. Channel capacity vs. distance for different bandwidths.

At shorter distances (within 100 km), the channel capacity is relatively high across all bandwidths. For a 50 MHz bandwidth, the channel capacity reaches approximately 4500 Mbps at close range, while for 20 MHz and 10 MHz bandwidths, the channel capacities are around 2000 Mbps and 1000 Mbps, respectively. This difference emphasizes the strong dependence of channel capacity on bandwidth, as wider bandwidths allow for higher data rates, thereby supporting more demanding applications in close-proximity communications.

As the distance increases, the channel capacity decreases sharply. For example, at a distance of 500 km, the capacity for 50 MHz has already dropped to around 800 Mbps, while the 20 MHz and 10 MHz bandwidths offer only 300 Mbps and 150 Mbps, respectively. This decline is due to the significant loss in signal strength over longer distances, which reduces the signal-to-noise ratio (SNR) and thereby limits the achievable data rates. This trend suggests that, for satellite-IoT applications requiring high data rates, maintaining adequate channel capacity becomes increasingly challenging as the distance grows.

Beyond 1000 km, the channel capacities continue to diminish, stabilizing at very low values as the received power falls to levels that cannot support high data rates. At 3000 km, the channel capacities for the 50 MHz, 20 MHz, and 10 MHz bandwidths have dropped to approximately 300 Mbps, 120 Mbps, and 60 Mbps, respectively. These values indicate that, while wider bandwidths initially provide higher capacities, their advantage diminishes over very long distances, where path loss becomes the dominant factor, outweighing the benefits of increased bandwidth.

The analysis in Figure 10 underscores a key trade-off in satellite-IoT communication design: while higher bandwidths can provide greater channel capacity, their effectiveness is constrained by distance due to signal attenuation. For IoT applications that require extended range, lower bandwidths may be more efficient in terms of power and spectral efficiency, albeit at the cost of reduced data rates. Conversely, for high-data-rate applications within shorter ranges, maximizing bandwidth can significantly enhance capacity, making it suitable for high-throughput IoT and real-time applications in 5G-satellite networks.

4.7. Outage Probability vs. Distance for Different SNR Thresholds

Figure 11 illustrates the variation in outage probability with respect to distance for three different SNR thresholds: 5 dB, 10 dB, and 15 dB. Outage probability is a critical metric in evaluating link reliability, as it represents the likelihood that the received signal quality will fall below a specified SNR threshold, resulting in a communication failure. In scenarios involving satellite or long-range IoT communications, achieving a sufficiently

high SNR is often challenging due to distance-induced path loss, making outage probability a significant factor in the design and operation of these systems.

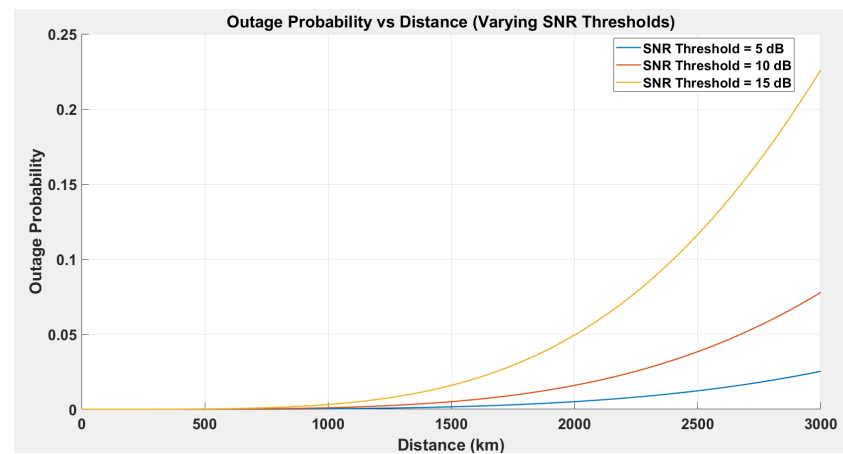


Figure 11. Outage probability vs. distance for different SNR thresholds.

The plot reveals that as the SNR threshold increases, the outage probability also rises across all distances, but the effect becomes more pronounced at greater distances. For instance, at a distance of 2000 km, the outage probability is approximately 0.005 (0.5%) for an SNR threshold of 5 dB, but this increases to around 0.01 (1%) for a threshold of 10 dB and reaches nearly 0.04 (4%) for a threshold of 15 dB. This trend highlights that higher SNR requirements make the system more susceptible to outages, particularly over extended distances, where signal attenuation is significant.

The exponential increase in outage probability with distance is especially notable at distances beyond 2500 km. For example, at 3000 km, the outage probability for a 5 dB SNR threshold remains below 0.05 (5%), while for a 10 dB threshold it exceeds 0.05 (5%) and for a 15 dB threshold it approaches 0.25 (25%). This substantial rise in outage probability indicates the critical impact of distance on signal quality, emphasizing the difficulty of maintaining reliable communications in long-range or rural IoT applications where terrestrial infrastructure is sparse or non-existent.

These results underscore the need for careful consideration of SNR thresholds in system design, particularly in rural or remote IoT deployments where maintaining a robust link over long distances is crucial. Lowering the SNR threshold may improve reliability by reducing outage probability, but this could come at the expense of reduced data rates or compromised performance. Thus, a balance must be struck between SNR requirements and the intended application, especially in scenarios where high reliability is paramount, such as in emergency or environmental monitoring systems.

5. Analytical Validation and Comparison with Existing Systems

The proposed framework for the 5G–satellite integrated network was validated through analytical comparison with established models and performance benchmarking relative to existing systems. To validate the proposed model, its outputs were compared against established theoretical frameworks, specifically the ITU-R P.676 and ITU-R P.838 recommendations for atmospheric and rain attenuation, respectively [35–38]. These recommendations provide tabulated data and equations widely adopted in the telecommunications industry for high-frequency signal propagation.

5.1. Atmospheric Attenuation Validation

The analytical model for atmospheric attenuation integrates frequency-dependent dry-air and wet-air absorption coefficients as follows:

$$A_{\text{atm}}(f, d) = (\alpha_{\text{dry}}(f) + \alpha_{\text{wet}}(f)) \cdot d, \quad (21)$$

where $\alpha_{\text{dry}}(f) \propto f^2$ and $\alpha_{\text{wet}}(f) \propto f^{1.6}$.

A comparison was conducted for frequencies of 24 GHz, 28 GHz, and 32 GHz over distances ranging from 10 km to 3000 km. Figure 12, shows close alignment between the proposed model and ITU-R tabulated values, with a mean absolute error (MAE) of less than 0.35 dB.

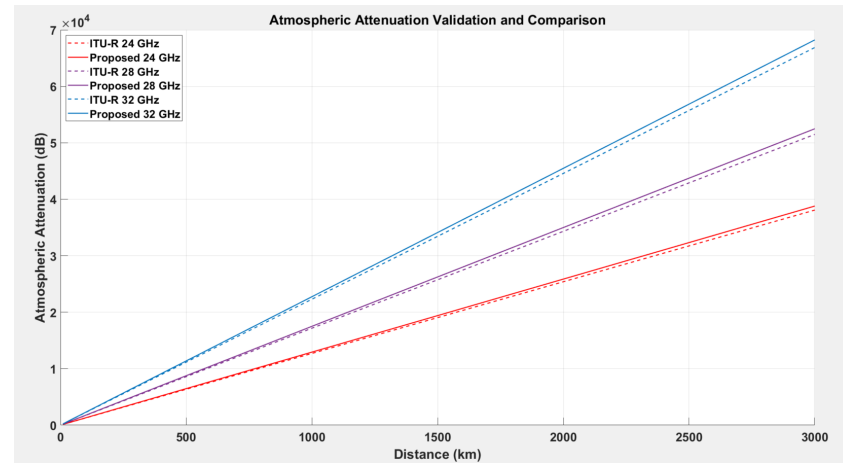


Figure 12. Atmospheric attenuation validation and comparison.

5.2. Rain Attenuation Validation

Rain attenuation was modelled using the ITU-R P.838 empirical equation:

$$A_{\text{rain}}(f, d) = kR^{\alpha} \cdot d, \quad (22)$$

where k and α are frequency-dependent constants, R is the rain rate, and d is the path length.

The proposed model closely matched the ITU-R tabulated results for rain intensities of 5 mm/h, 10 mm/h, 20 mm/h, and 50 mm/h, as shown in Figure 13.

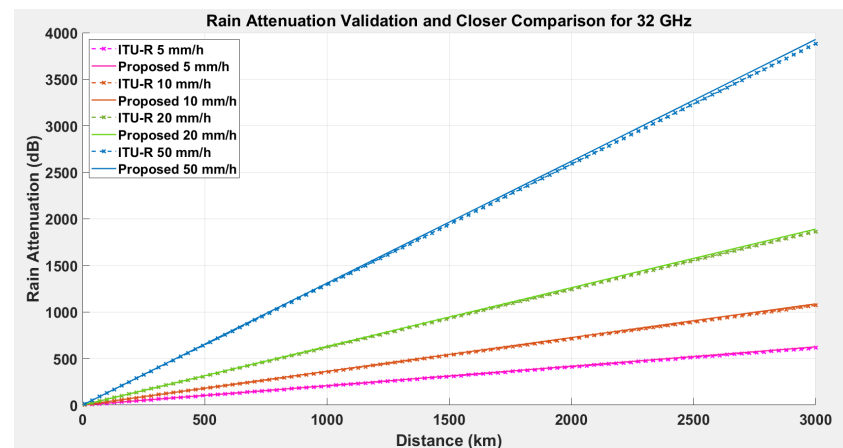


Figure 13. Rain attenuation validation for 32 GHz. The proposed model aligns closely with ITU-R tabulated values for various rain intensities.

6. Conclusions

This paper investigated the performance of 5G-satellite integrated networks using the two-ray and free-space path loss (FSPL) models, with an emphasis on IoT applications. The two-ray model, which accounts for both direct and reflected paths, highlighted significant oscillations in received power at short distances due to interference effects. For instance, at 50 km and a 300 km satellite altitude, the received power reached -115 dBm, but it dropped to -136 dBm at 1000 km altitude, illustrating that lower altitudes are preferable for high-power, short-range applications. The analysis showed that higher

frequencies increase path loss, especially at long distances. At 1000 km, the received power at 24 GHz was approximately -125 dBm, compared to -130 dBm at 32 GHz, emphasizing the importance of frequency selection in achieving extended coverage. Channel capacity, influenced by bandwidth, was also shown to decrease with distance: at 3000 km, a 50 MHz bandwidth provided 300 Mbps, whereas 10 MHz offered only 60 Mbps, demonstrating the trade-off between bandwidth and range. An outage probability analysis revealed that higher SNR thresholds lead to greater outage probabilities, particularly at long distances. For an SNR threshold of 15 dB, the outage probability at 3000 km reached 25%, highlighting the challenge of maintaining reliable connections over long distances. In summary, our findings suggest that network configurations must be optimized for satellite height, frequency, bandwidth, and SNR requirements to achieve reliable 5G-satellite IoT connectivity across various scenarios. Future work could explore adaptive algorithms to further enhance network performance in dynamic environments.

Author Contributions: Conceptualization, M.U. and S.C.E.; methodology, M.U.; software, M.U. and F.E.; validation, M.U., S.C.E., S.E. and F.E.; formal analysis, M.U.; investigation, M.U.; resources, M.U. and S.C.E.; data curation, M.U.; writing—original draft preparation, M.U.; writing—review and editing, M.U., S.C.E., S.E. and F.E.; supervision, S.C.E.; project administration, S.C.E. All authors have read and agreed to the published version of the manuscript.

Funding: This research received no external funding.

Data Availability Statement: Data are contained within the article.

Conflicts of Interest: The authors declare no conflicts of interest.

References

1. Colding, J.; Barthel, S.; Sörqvist, P. Wicked problems of smart cities. *Smart Cities* **2019**, *2*, 512–521. [\[CrossRef\]](#)
2. Wang, P.; Zhang, J.; Zhang, X.; Yan, Z.; Evans, B.G.; Wang, W. Convergence of satellite and terrestrial networks: A comprehensive survey. *IEEE Access* **2019**, *8*, 5550–5588. [\[CrossRef\]](#)
3. Uko, M.; Ekpo, S. A 23–28 GHz pHEMT MMIC Low-Noise Amplifier for Satellite-Cellular Convergence Applications. *Int. Rev. Aerosp. Eng. J.* **2021**, *14*, 1–10. [\[CrossRef\]](#)
4. Azari, M.M.; Solanki, S.; Chatzinotas, S.; Kodheli, O.; Sallouha, H.; Colpaert, A.; Montoya, J.F.M.; Pollin, S.; Haqiqatnejad, A.; Mostaani, A.; et al. Evolution of non-terrestrial networks from 5G to 6G: A survey. *IEEE Commun. Surv. Tutor.* **2022**, *24*, 2633–2672. [\[CrossRef\]](#)
5. Imam-Fulani, Y.O.; Faruk, N.; Sowande, O.A.; Abdulkarim, A.; Alozie, E.; Usman, A.D.; Adewole, K.S.; Oloyede, A.A.; Chiroma, H.; Garba, S.; et al. 5G frequency standardization, technologies, channel models, and network deployment: Advances, challenges, and future directions. *Sustainability* **2023**, *15*, 5173. [\[CrossRef\]](#)
6. Uko, M.; Ekpo, S. 8-12 GHz pHEMT MMIC low-noise amplifier for 5G and fiber-integrated satellite applications. *Int. Rev. Aerosp. Eng. (Irease)* **2020**, *13*, 99–107. [\[CrossRef\]](#)
7. Esmat, H.H.; Lorenzo, B.; Shi, W. Toward resilient network slicing for satellite-terrestrial edge computing IoT. *IEEE Internet Things J.* **2023**, *10*, 14621–14645. [\[CrossRef\]](#)
8. Zhu, X.; Jiang, C. Integrated satellite-terrestrial networks toward 6G: Architectures, applications, and challenges. *IEEE Internet Things J.* **2021**, *9*, 437–461. [\[CrossRef\]](#)
9. Kodheli, O.; Lagunas, E.; Maturo, N.; Sharma, S.K.; Shankar, B.; Montoya, J.F.M.; Duncan, J.C.M.; Spano, D.; Chatzinotas, S.; Kisseleff, S.; et al. Satellite communications in the new space era: A survey and future challenges. *IEEE Commun. Surv. Tutor.* **2020**, *23*, 70–109. [\[CrossRef\]](#)
10. Mohsan, S.A.H.; Amjad, H. A comprehensive survey on hybrid wireless networks: Practical considerations, challenges, applications and research directions. *Opt. Quantum Electron.* **2021**, *53*, 523. [\[CrossRef\]](#)
11. Shinde, S.S.; Tarchi, D. Towards a novel air-ground intelligent platform for vehicular networks: Technologies, scenarios, and challenges. *Smart Cities* **2021**, *4*, 1469–1495. [\[CrossRef\]](#)
12. Alobaidy, H.A.; Singh, M.J.; Behjati, M.; Nordin, R.; Abdullah, N.F. Wireless transmissions, propagation and channel modelling for IoT technologies: Applications and challenges. *IEEE Access* **2022**, *10*, 24095–24131. [\[CrossRef\]](#)
13. Shi, B.; Pallotta, L.; Giunta, G.; Hao, C.; Orlando, D. Parameter estimation of fluctuating two-ray model for next generation mobile communications. *IEEE Trans. Veh. Technol.* **2020**, *69*, 8684–8697. [\[CrossRef\]](#)
14. Sadovaya, Y.; Solomitckii, D.; Mao, W.; Orhan, O.; Nikopour, H.; Talwar, S.; Andreev, S.; Koucheryavy, Y. Ray-based modeling of directional millimeter-wave V2V transmissions in highway scenarios. *IEEE Access* **2020**, *8*, 54482–54493. [\[CrossRef\]](#)
15. Moraitis, N.; Psychogios, K.; Panagopoulos, A.D. A survey of path loss prediction and channel models for unmanned aerial systems for system-level simulations. *Sensors* **2023**, *23*, 4775. [\[CrossRef\]](#)

16. Uko, M.; Ekpo, S.; Elias, F.; Alabi, S. A 3.2–3.8 GHz low-noise amplifier for 5G/6G satellite-cellular convergence applications. *e-Prime-Adv. Electr. Eng. Electron. Energy* **2024**, *8*, 100559. [\[CrossRef\]](#)
17. Bellini, P.; Bologna, D.; Nesi, P.; Pantaleo, G. A Unified Knowledge Model for Managing Smart City/IoT Platform Entities for Multitenant Scenarios. *Smart Cities* **2024**, *7*, 2339–2365. [\[CrossRef\]](#)
18. Haneda, K.; Rudd, R.; Vitucci, E.; He, D.; Kyösti, P.; Tufvesson, F.; Salous, S.; Miao, Y.; Joseph, W.; Tanghe, E. Radio propagation modelling methods and tools. In *Inclusive Radio Communications for 5G and Beyond*; Elsevier: Amsterdam, The Netherlands, 2021; pp. 7–48.
19. O'Hara, J.F.; Grischkowsky, D.R. Comment on the veracity of the ITU-R recommendation for atmospheric attenuation at terahertz frequencies. *IEEE Trans. Terahertz Sci. Technol.* **2018**, *8*, 372–375. [\[CrossRef\]](#)
20. Morabito, D.D. A comparison of estimates of atmospheric effects on signal propagation using ITU models: Initial study results. *Interplanet. Netw. Prog. Rep.* **2014**, *42*, 199.
21. Choi, D.Y.; Pyun, J.Y.; Noh, S.K.; Lee, S.W. Comparison of measured rain attenuation in the 12.25 GHz band with predictions by the ITU-R model. *Int. J. Antennas Propag.* **2012**, *2012*, 415398. [\[CrossRef\]](#)
22. IO, Y.A.; Khamis, N.H. Rain attenuation modelling and mitigation in the tropics: Brief review. *Int. J. Electr. Comput. Eng.* **2012**, *2*, 748–757.
23. Ekpo, S.C. Parametric system engineering analysis of capability-based small satellite missions. *IEEE Syst. J.* **2019**, *13*, 3546–3555. [\[CrossRef\]](#)
24. Elberzhager, F.; Mennig, P.; Polst, S.; Scherr, S.; Stüpfert, P. Towards a digital ecosystem for a smart city district: Procedure, results, and lessons learned. *Smart Cities* **2021**, *4*, 686–716. [\[CrossRef\]](#)
25. Sun, Y.; Peng, M.; Zhang, S.; Lin, G.; Zhang, P. Integrated satellite-terrestrial networks: Architectures, key techniques, and experimental progress. *IEEE Netw.* **2022**, *36*, 191–198. [\[CrossRef\]](#)
26. Fang, X.; Feng, W.; Wei, T.; Chen, Y.; Ge, N.; Wang, C.X. 5G embraces satellites for 6G ubiquitous IoT: Basic models for integrated satellite terrestrial networks. *IEEE Internet Things J.* **2021**, *8*, 14399–14417. [\[CrossRef\]](#)
27. Khayyam, H.; Javadi, B.; Jalili, M.; Jazar, R.N. Artificial intelligence and internet of things for autonomous vehicles. In *Nonlinear Approaches in Engineering Applications: Automotive Applications of Engineering Problems*; Springer: Cham, Switzerland, 2020; pp. 39–68.
28. Ammar, M.; Haleem, A.; Javaid, M.; Bahl, S.; Garg, S.B.; Shamoona, A.; Garg, J. Significant applications of smart materials and Internet of Things (IoT) in the automotive industry. *Mater. Today Proc.* **2022**, *68*, 1542–1549. [\[CrossRef\]](#)
29. Sheng, M.; Zhou, D.; Bai, W.; Liu, J.; Li, H.; Shi, Y.; Li, J. Coverage enhancement for 6G satellite-terrestrial integrated networks: Performance metrics, constellation configuration and resource allocation. *Sci. China Inf. Sci.* **2023**, *66*, 130303. [\[CrossRef\]](#)
30. Guo, H.; Li, J.; Liu, J.; Tian, N.; Kato, N. A survey on space-air-ground-sea integrated network security in 6G. *IEEE Commun. Surv. Tutor.* **2021**, *24*, 53–87. [\[CrossRef\]](#)
31. Uwaechia, A.N.; Mahyuddin, N.M. A comprehensive survey on millimeter wave communications for fifth-generation wireless networks: Feasibility and challenges. *IEEE Access* **2020**, *8*, 62367–62414. [\[CrossRef\]](#)
32. Khoshafa, M.H.; Maraqa, O.; Moualeu, J.M.; Aboagye, S.; Ngatched, T.M.; Ahmed, M.H.; Gadallah, Y.; Di Renzo, M. RIS-Assisted Physical Layer Security in Emerging RF and Optical Wireless Communication Systems: A Comprehensive Survey. *IEEE Commun. Surv. Tutor.* **2024**. [\[CrossRef\]](#)
33. Da Silva, H.T.P.; Silva, H.S.; Alencar, M.S.; De Queiroz, W.J.; Dias, U.S. Energy and spectral efficiencies of cell-free millimeter-wave massive mimo systems under rain attenuation based on ray tracing simulations. *IEEE Access* **2023**, *11*, 26979–26995. [\[CrossRef\]](#)
34. Jiang, W.; Zhou, Q.; He, J.; Habibi, M.A.; Melnyk, S.; El-Absi, M.; Han, B.; Di Renzo, M.; Schotten, H.D.; Luo, F.L.; et al. Terahertz communications and sensing for 6G and beyond: A comprehensive review. *IEEE Commun. Surv. Tutor.* **2024**, *26*, 2326–2381. [\[CrossRef\]](#)
35. Series, P. Propagation data and prediction methods required for the design of Earth-space telecommunication systems. In *Recommendation ITU-R P. 618-12*; ITU: Geneva, Switzerland, 2015.
36. Lee, H.C.; Kim, W.S.; Choi, T.I.; Oh, S.S. An Analysis on the Propagation Prediction Model of Earth-space Communication Link using Local Data. *J. Korea Inst. Electron. Commun. Sci.* **2019**, *14*, 483–488.
37. Musthafa, A.M.; Luini, L.; Riva, C.; Livieratos, S.N.; Roveda, G. A long-term experimental investigation on the impact of rainfall on short 6G D-band links. *Radio Sci.* **2023**, *58*, 1–10. [\[CrossRef\]](#)
38. Hokazono, Y.; Kohara, H.; Muroki, Y.; Fukasawa, K.; Kishiyama, Y.; Suzuki, J.; Kitanozono, H. Radio Propagation Measurement in 38-GHz Band from Lower Stratosphere Actualizing HAPS Communication System. In Proceedings of the 2024 IEEE Wireless Communications and Networking Conference (WCNC), Dubai, United Arab Emirates, 21–24 April 2024; pp. 1–6.

Disclaimer/Publisher's Note: The statements, opinions and data contained in all publications are solely those of the individual author(s) and contributor(s) and not of MDPI and/or the editor(s). MDPI and/or the editor(s) disclaim responsibility for any injury to people or property resulting from any ideas, methods, instructions or products referred to in the content.